Progress In Electromagnetics Research M, Vol. 102, 13–26, 2021

Scattering Characteristics of Ultra-High-Voltage Power Lines in Spaceborne SAR Images

Shuzhu Shi[1, *], Ailing Hou[2], Yan Liu[3], Lei Cheng[3], and Zhiwei Chen[3]

Abstract—Owing to its all-day and all-weather imaging capabilities, high-resolution spaceborne synthetic aperture radar has shown great potential for the effective monitoring of wide-area, ultra-high-voltage (UHV) transmission lines. Scattering characteristics of UHV power lines in 3-m-resolution TerraSAR-X images is analyzed in this paper. First, the study area and structure of the UHV transmission line are introduced. Then, the data processing method is described, which includes the preprocessing of TerraSAR-X images and target feature extraction. Finally, the scattering characteristics of the UHV power line are analyzed, and the analysis results demonstrate that the UHV power line can be visible in a TerraSAR-X image only when the angle between its extension direction and the azimuth of the sub-satellite ground track is within ±15°. Furthermore, besides the span length, the spatial location of the UHV power line in a TerraSAR-X image is also influenced by the angle between its extension direction and the azimuth of the sub-satellite ground track, as well as by the height difference between adjacent pylons.

1. INTRODUCTION

Owing to the obvious advantages of improving transmission capacity, increasing power transmission distance, reducing line losses, lowering project investment, and reducing the land occupation of power lines, many ultra-high-voltage (UHV) transmission lines, which have a total length of more than 30,000 km, have been built to transfer the electric power from the northwest and southwest regions to relatively developed central and eastern regions due to the imbalance distribution of energy resources and loads in China [1]. Furthermore, for some areas through which a UHV transmission line passes, the climate is diverse, and natural disasters occur frequently. As a result, effective monitoring of UHV power lines is very important for the safe and reliable operation of UHV transmission lines.

In recent years, a variety of sensors have been exploited to remotely inspect power lines, such as camera and video devices carried by unmanned aerial vehicles [2] or low-Earth-orbiting satellites [3], airborne light detection and ranging systems [4], and airborne millimeter-wave radars [5]. As an active microwave imaging sensor, synthetic aperture radar (SAR) can provide high-resolution images for wide-area monitoring in all-day and all-weather conditions, which makes it particularly interesting for applications like remote sensing of transmission lines in adverse weather conditions [6]. For example, UHV power lines can be damaged by both freezing precipitation and typhoons. However, the observation performance of the aforementioned sensors is seriously reduced under such weather conditions, except for airborne and spaceborne SARs [7]. It is worth mentioning here that we only considered the spaceborne SAR images because the airborne SAR images over the study area were not acquired. Therefore, it can be found that spaceborne SAR has shown great potential for the effective monitoring of wide-area UHV power lines. With the continuous improvement of the spatial resolution of spaceborne SAR, the

---

Received 7 February 2021, Accepted 26 March 2021, Scheduled 1 April 2021

* Corresponding author: Shuzhu Shi (shishuzhu@whu.edu.cn).

[1] School of Remote Sensing and Information Engineering, Wuhan University, Wuhan 430079, China. [2] Global Navigation Satellite Systems Research Center, Wuhan University, Wuhan 430079, China. [3] State Key Laboratory of Power Grid Environmental Protection, China Electric Power Research Institute, Wuhan 430074, China.

detection of high-voltage transmission lines based on high-resolution spaceborne SAR images has become possible, and several related studies have been reported. Schwarz et al. [8] illustrated, with a figure, how a pylon was visible in the time-frequency decomposition results of a TerraSAR-X image. Liu et al. [9, 10] found that both pylons and power lines in UHV or extra-high-voltage (EHV) transmission lines can be detected in high-resolution COSMO-SkyMed and TerraSAR-X images, even if the pylon has frozen [11]. Li et al. [12] and Chen et al. [13] further analyzed the scattering characteristics of EHV power lines using time-series TerraSAR-X images. The results of their studies showed that the spatial location of EHV power lines in a TerraSAR-X image was influenced by the temperature, and the phase of bright spots produced by EHV power lines was unstable in time-series TerraSAR-X images. It should be noted that since the structure and cable diameter of a UHV power line are different from those of an EHV power line [14], their scattering characteristics in spaceborne SAR images are also different. Tao and Liu [15] proposed a simulation model for high-resolution spaceborne SAR when it was used to monitor a transmission line with an extension direction running from south to north. In a recent study [16], it was found that the spatial location of the UHV power line in a TerraSAR-X image was also influenced by the span length, and the intensity of the bright spots produced by the power line was affected by radar polarization. However, a comprehensive investigation of the scattering characteristics of UHV power lines in spaceborne SAR images is still on-going because they are simultaneously influenced by many factors, including span length, ambient temperature, and radar polarization, as mentioned above. Nevertheless, this study is important for developing the algorithms used to automatically monitor power lines based on spaceborne SAR images, similar to those works performed to extract power lines from airborne SAR images [17, 18].

In this paper, the scattering characteristics of UHV power lines in 3-m-resolution TerraSAR-X images are presented. The rest of this paper is organized as follows. The study area and structure of UHV transmission line are first introduced in Section 2. Next, the data processing method is described in Section 3, which includes the preprocessing of TerraSAR-X images and target feature extraction. Scattering characteristics of UHV power lines in TerraSAR-X images are described in Section 4 and discussed in Section 5. Finally, conclusions are given in Section 6.

2. STUDY AREA

The 1000-kV Jindongnan-Nanyang-Jingmen UHV alternating current test and demonstration project, which was put into operation on January 6, 2009, is the first UHV transmission line in commercial operation in the World. It starts from Jindongnan Substation in Changzi of Shanxi Province, via Nanyang switching station in Nanyang of Henan Province, and ends at Jingmen substation in Jingmen of Hubei Province [19]. The overall length of this project is approximately 640 km, and the line is single circuit with 1,275 pylons [20]. This UHV transmission line in Hubei Province, whose location is approximately 112°–113°E longitude and $30^\circ 30'$–$32^\circ 30'$N latitude, was chosen as the study area, as indicated by the black bold line in Fig. 1. In addition, the coverage of three TerraSAR-X images used to monitor the UHV power lines is also marked by the blue rectangles in Fig. 1.

In practical observations, a total of 151 pylons and 150 sections of power lines were covered by the adopted TerraSAR-X images. A photograph of the Jindongnan-Nanyang-Jingmen UHV transmission line in Hubei Province is presented in Fig. 2. Three conductor bundles and two ground wires are hung on a cat-head-shaped pylon. Here, three conductor bundles hung on the lower portion of the pylon are arranged in triangular configuration, while two ground wires hung on the upper portion of the pylon are arranged in a horizontal configuration.

Figure 3 shows the structure of conductor bundles, a sub-conductor, and a ground wire. A conductor bundle consists of eight steel-reinforced aluminum sub-conductors of type LGJ-500/35, as shown in Fig. 3(a). Furthermore, the eight-subconductor bundle is arranged as a regular octagon with a circumcircle diameter of 1045 mm, and the distance between adjacent sub-conductors is 400 mm. Fig. 3(b) shows that a sub-conductor consists of 48 aluminum cores and seven steel cores. Its diameter is 30 mm, and the diameter of an aluminum core is 2.4 mm. In addition, one ground wire is a JLB20A-170type aluminum sheathed stranded conductor that operates in the mode of subsection insulation and single-point grounding, and the other is an optical power ground wire (OPGW) that is grounded on each pylon. Moreover, the diameter of each ground wire is 17 mm, as shown in Fig. 3(c).

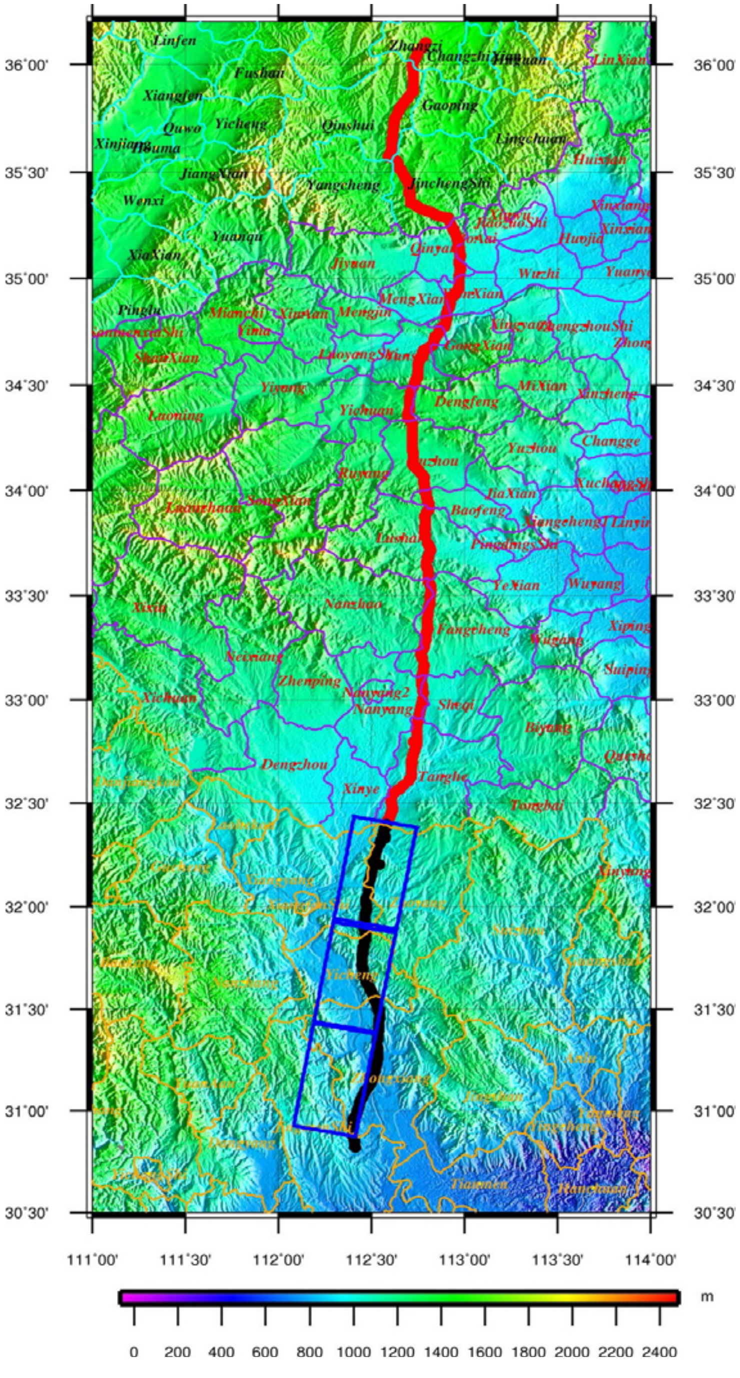

Figure 1. Sketch map of the Jindongnan-Nanyang-Jingmen ultra-high-voltage (UHV) transmission line, which is marked by the bold line. Black bold line denotes this UHV transmission line in Hubei Province and was chosen as our study area. In addition, blue rectangles represent coverage of three TerraSAR-X images used to monitor UHV power lines.

3. DATA PROCESSING METHOD

The data processing method in the present study mainly includes preprocessing of TerraSAR-X images and scattering feature extraction of UHV power lines. A flowchart of the data processing method is shown in Fig. 4, and each step is described below.

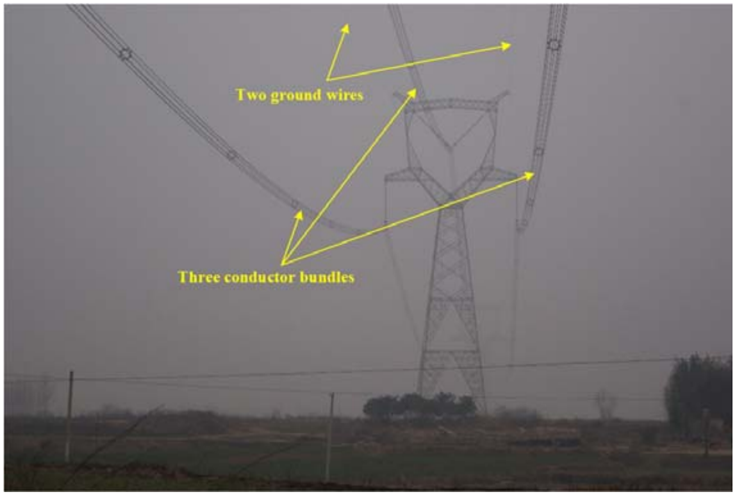

Figure 2. Photograph of Jindongnan-Nanyang-Jingmen UHV transmission line in Hubei Province. Three conductor bundles and two ground wires are hung on the cat-head-shaped pylon.

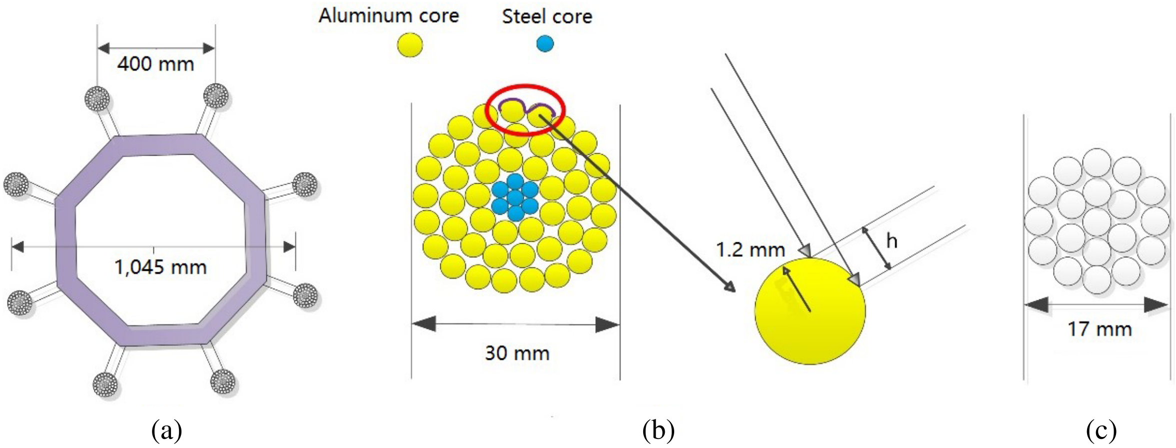

Figure 3. Structure of (a) 8 × LGJ-500/35 conductor bundles, (b) sub-conductor, and (c) ground wire.

3.1. Preprocessing of TerraSAR-X images

Table 1 provides the main characteristics of these TerraSAR-X images used to observe the Jindongnan-Nanyang-Jingmen UHV transmission line in Hubei Province. Furthermore, the Single-look Slant-range Complex (SSC) products were used, and one parameter acquired from the SSC products is intensity. Since the intensity is related to the object of interest, it was used to identify the UHV pylons and power lines from TerraSAR-X images. Moreover, the texture information, obtained from the intensity image, was used to further improve the identification of pylons and power lines. Additional details of the TerraSAR-X SSC products can be found in [21].

The first step in the preprocessing of TerraSAR-X SSC products is to generate the corresponding intensity map, in which the intensity is expressed in decibel values. Then, the terrain correction is applied to SSC products to remove image distortions that are caused by the varying terrain height, as shown in Fig. 1. Here, the intensity map was geometrically corrected using the Shuttle Radar Topography Mission (SRTM) Digital Elevation Model (DEM). To analyze the spatial location of the UHV power line in TerraSAR-X images, these corrected images were further resampled and projected to the World Geodetic System 1984 (WGS84) reference ellipsoid to obtain geocoded images. However, when these geocoded images were overlaid on Google Earth, obvious offsets between them were found

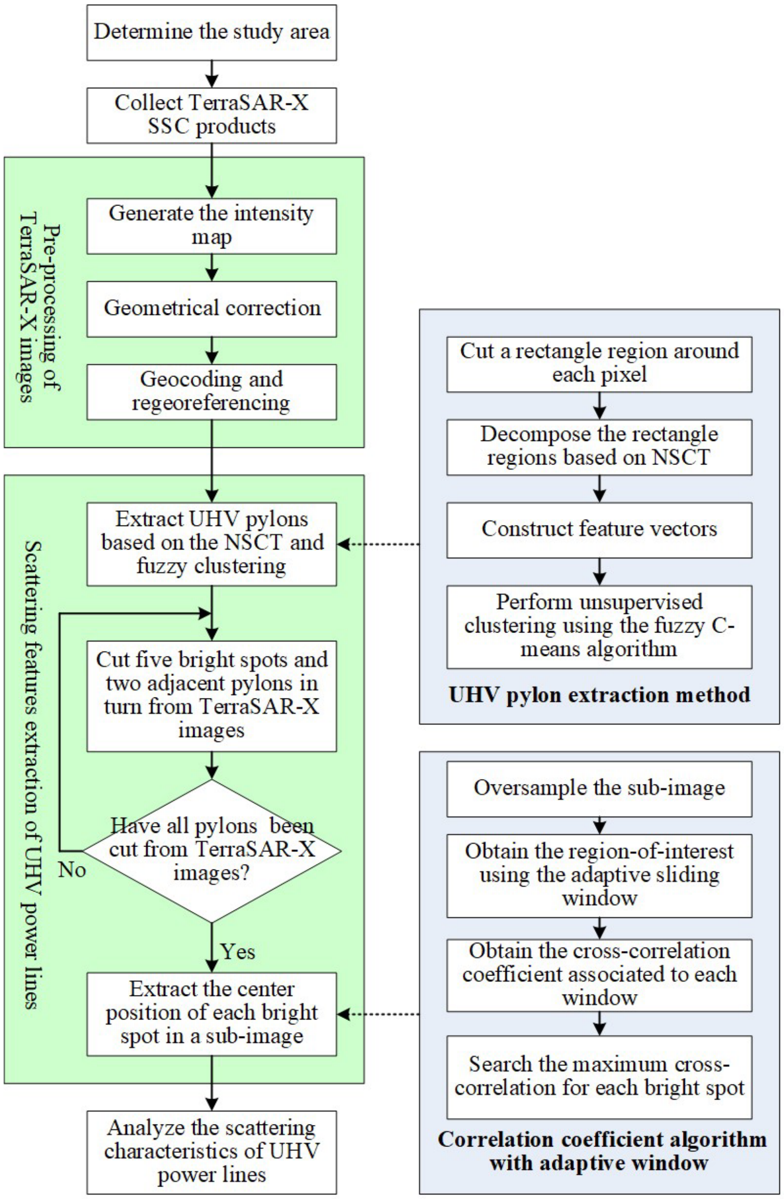

Figure 4. Flowchart of data processing method.

which caused the bright spots produced by the UHV power line to not be located between adjacent pylons. Therefore, the geocoding information of the obtained images was further corrected using 10 ground control points on Google Earth images, including the top corner of buildings and the cross-section of bedrocks, due to their stability and ease of identification. It is worth mentioning here that the speckle noise was not mitigated because the size of a UHV power line in TerraSAR-X images is smaller than the spatial resolution given in Table 1. Furthermore, traditional methods used to mitigate the speckle noise can degrade the image resolution and suppress the peak of the echo signal, such as multi-looking and speckle filtering.

3.2. Scattering Feature Extraction of Power Line

After the aforementioned preprocessing of TerraSAR-X images, both UHV pylons and power lines can be clearly seen in imagery, as shown in Fig. 5. It can be found that the shape of a cat-head-shaped pylon in TerraSAR-X images is a triangle. Moreover, five bright spots are located between adjacent

Table 1. Main characteristics of TerraSAR-X images obtained over study area.

Item	Specification
Orbit	Descending
Radar wavelength	31.2 mm
Incidence angle	29.7°
Imaging mode	Stripmap
Spatial resolution	3 m
Scene size	30 km × 50 km (width × height)
Polarization	Horizontal-horizontal, vertical-vertical
Quantity	3
Acquisition date	July 24, 2018

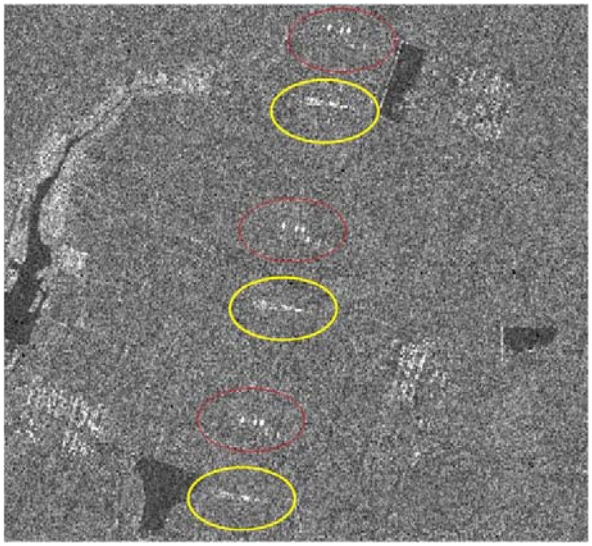

Figure 5. UHV pylons and power lines appearing in a TerraSAR-X image. Five bright spots highlighted by red ellipses are produced by three conductor bundles and two ground wires. In addition, UHV pylons are highlighted by yellow ellipses.

cat-head-shaped pylons. Here, three spots near the upper portion are generated by the three conductor bundles, while two spots near the lower portion are produced by the two ground wires.

Since a pylon can be more easily identified from TerraSAR-X images than a power line, UHV pylons were extracted using an algorithm based on the Non-Subsampled Contourlet Transform (NSCT) and fuzzy clustering. In this algorithm, first, each pixel is chosen in turn as the center. Then, a rectangular region is cut from the preprocessed image around this center. Here, the size of the rectangular region is set to 8×8 pixels. Subsequent to this step, the NSCT is used to decompose this rectangular region into four directional subbands at two scales. Furthermore, both the first-order statistical features and co-occurrence matrix in the NSCT domain are extracted to construct feature vectors. Based on the feature vectors, a fuzzy C-means clustering algorithm [22] was applied to perform the unsupervised clustering, and the final target extraction results are provided based on these clustering results. In practice, a total of 151 UHV pylons were extracted from the obtained TerraSAR-X images using the aforementioned algorithm.

Figure 5 shows that five bright spots produced by the three conductor bundles and two ground wires are located between adjacent pylons. Therefore, they were, in turn, cut from TerraSAR-X images

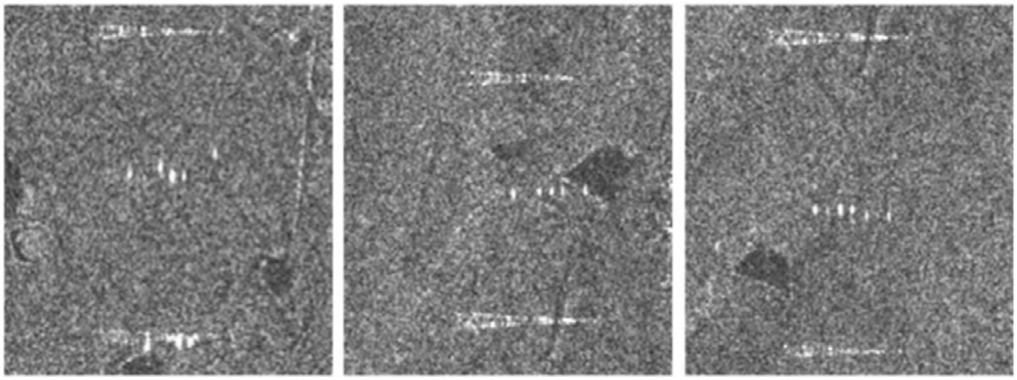

Figure 6. Three sub-images that were cut from TerraSAR-X images. Each sub-image includes five bright spots and two adjacent pylons.

for further analysis, in conjunction with adjacent pylons, as shown in Fig. 6. In principle, 150 groups of bright spots should be obtained, but, in practice, only 116 groups of bright spots were extracted from the TerraSAR-X images because the other 34 sections of power lines did not produce corresponding bright spots.

In addition, Fig. 6 shows the irregular shape of the bright spots. Moreover, the size of each bright spot changes randomly. For example, the sizes of the bright spots produced by three conductor bundles range between 6 and 47 pixels, while the sizes of those generated by two ground wires vary between 7 and 18 pixels. Therefore, a correlation coefficient method with adaptive window was employed to extract the center position of each bright spot in a sub-image. In this method, the sub-image was first oversampled 16 times to achieve finer position result for each bright spot. Following this step, the impulse response function of a point target in the SAR imaging can be described by [23]

$$\operatorname{sinc}(x, y) = (\sin(\pi x)/\pi x) \times (\sin(\pi y)/\pi y)\,. \tag{1}$$

Furthermore, the above two-dimensional sinc function can be used to cross-correlate with a SAR image, and the position of a point target in this SAR image can be further extracted in terms of the obtained cross-correlation coefficient [24]. Meanwhile, the bright spots produced by power lines are similar to those generated by point targets in a SAR image. Therefore, an adaptive sliding window was adopted to obtain the region-of-interest (ROI), and then the two-dimensional sinc function given in Equation (1) was used to cross-correlate with the ROI to obtain the cross-correlation coefficient associated with each window. Here, the size of the sliding window increased from 1 pixel to the maximum search area in terms of the obtained cross-correlation coefficient. It is worth mentioning here that the maximum search area should include the entire bright spot. Subsequently, the cross-correlation coefficients associated with each window were compared with each other to obtain the final maximum cross-correlation coefficient for each bright spot. Finally, the location of the maximum cross-correlation coefficient was chosen as the center position of the bright spot.

4. RESULTS

4.1. Intensity of Bright Spots

It can be seen from Fig. 6 that the intensity of the bright spots produced by the three conductor bundles is higher than that of those generated by the two ground wires. After a statistical analysis of the obtained 116 groups of bright spots, it was found that the intensity of these bright spots generated by the conductor bundles varied between 56 and 76 dBm, and the average value was 68.2 dBm. In contrast, the intensity of the bright spots produced by the ground wires ranged between 56 and 61 dBm, and the average value was 58.3 dBm. Therefore, the difference between average values of the two kinds of bright spots is 9.9 dB.

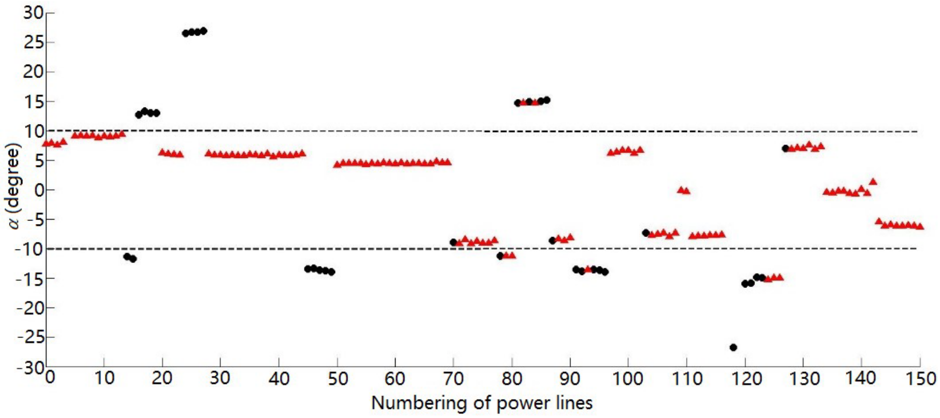

Figure 7. Relationship between generation of bright spots and angle α. Here, the red triangle and black circle denote that the bright spots were or were not produced by the power lines, respectively. α represents the angle between the extension direction of the power line and the azimuth of the sub-satellite ground track.

4.2. Generation Condition of Bright Spots

After a statistical analysis of the obtained 116 groups of bright spots, the relationship between the generation of bright spots and the angle α is depicted in Fig. 7. Here, α denotes the angle between the extension direction of the power line and the azimuth of the sub-satellite ground track. Taking the extension direction of the power line as a reference, when the sub-satellite ground track coincides with it, α equals 0°. When the sub-satellite ground track deviates from the extension direction of the power line in the counter-clockwise direction, α changes to a negative value. On the contrary, α is positive.

The following results can be gleaned from Fig. 7.

1) When $-10° \leq \alpha \leq 10°$, 110 sections of power lines were included in this case. Moreover, 106 sections of power lines produced corresponding bright spots, and only four sections of power lines did not generate them.
2) When $-15° \leq \alpha < -10°$ or $10° < \alpha \leq 15°$, 33 sections of power lines were included in this case. Moreover, only eight sections of power lines produced corresponding bright spots, while 25 sections of power lines did not generate them.
3) When $\alpha < -15°$ or $15° < \alpha$, seven sections of power lines were included in this case, and none of them produced bright spots.

4.3. Spatial Location of Bright Spots

For different values of α, Fig. 8 shows the variation of bright spot's spatial location in a TerraSAR-X image, and the following results can be obtained.

a) When α is approximately 0°, five bright spots are close to the perpendicular bisector of adjacent pylons, as shown in Fig. 8(c). When α decreases from 0° to $-10°$, five bright spots are close to the upper pylon, as shown in Figs. 8(a) and 8(b). When α increases from 0° to 10°, five bright spots are close to the lower pylon, as shown in Figs. 8(d) and 8(e).
b) Besides the extension direction of the power line, the spatial location of each bright spot also has an offset in the vertical direction of the power line. When α increases from $-10°$ to 4°, three bright spots produced by conductor bundles gradually move closer to these bright spots produced by the ground wires, as shown in Figs. 8(a)–8(d). On the contrary, when α increases from 4° to 10°, three bright spots produced by the conductor bundles are gradually away from these bright spots produced by the ground wires, as shown in Figs. 8(d) and 8(e).

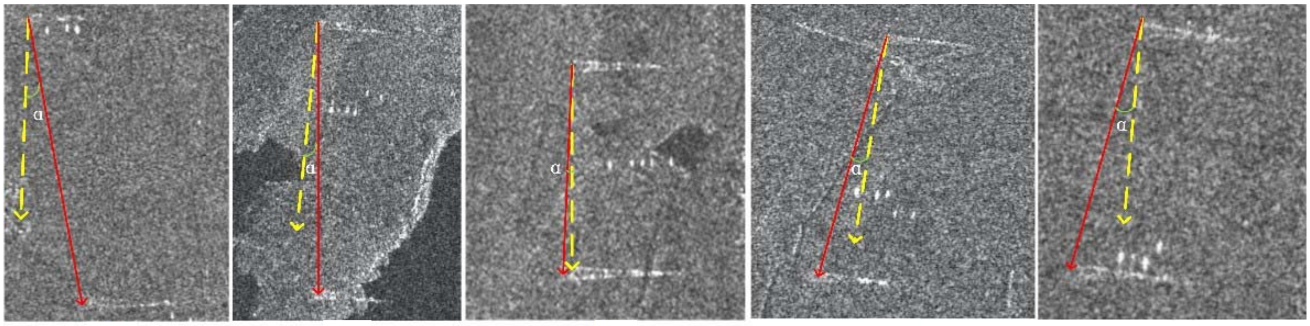

(a) (b) (c) (d) (e)

Figure 8. Variation of bright spot spatial position in a TerraSAR-X image for different values of α. Here, solid red and yellow dotted lines denote the extension direction of the power line and the azimuth of the sub-satellite ground track, respectively. Moreover, α is $-11.2°$, $-5.6°$, $0.06°$, $4.2°$, and $9.1°$ in subfigures (a)–(e), respectively.

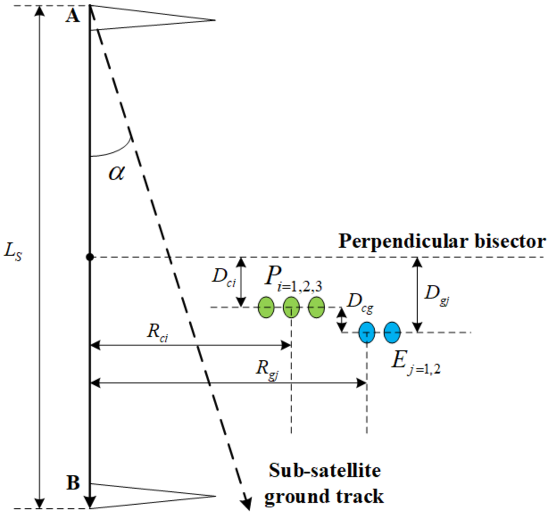

Figure 9. Simplified geometry of the subfigures shown in Fig. 8. Here, A and B denote two adjacent pylons.

A simplified geometry of these subfigures shown in Fig. 8 is introduced to quantify the spatial position of the bright spots, as depicted in Fig. 9, similar to that given in [16]. Moreover, the following parameters were added: L_S is the span length; $\overrightarrow{AB}$ represents the position vector between adjacent pylons, i.e., A and B; D_{ci} is the distance between the bright spot P_i and the perpendicular bisector of $\overrightarrow{AB}$; R_{ci} is the distance between the bright spot P_i and $\overrightarrow{AB}$, $i = 1, 2, 3$; D_{gj} is the distance between the bright spot E_j and the perpendicular bisector of $\overrightarrow{AB}$; R_{gj} is the distance between the bright spot E_j and $\overrightarrow{AB}$, $j = 1, 2$; D_{cg} is the difference between D_{ci} and D_{gj}; H_B and H_A denote the heights of the lower and upper pylons, respectively; and H_{BA} is the height difference between adjacent pylons, i.e., $H_{BA} = H_A - H_B$. In addition, a practically applicable assumption is made, i.e., D_{ci} and D_{gj} are positive when the bright spot is below the perpendicular bisector of $\overrightarrow{AB}$. On the contrary, D_{ci} and D_{gj} change to negative values.

For the sake of solidity, but without loss of generality, three typical cases were considered to conduct a quantitative analysis about how the spatial location of these bright spots in a TerraSAR-X image is influenced by the angle α, length L_S, and height difference H_{BA}, i.e., $\alpha \approx -9°$, $\alpha \approx 0°$, and $\alpha \approx 9°$,

Table 2. Offsets of bright spots produced by three conductor bundles in the extension direction of the power line when α is approximately $-9°$, $0°$, and $9°$.

Numbering of pylon B	Numbering of pylon A	$\alpha(°)$	H_{BA} (m)	L_S (m)	D_{ac}^1 (m)	D_{ag}^2 (m)
275	276	−9.08	0	607.6	−176	Non^3
278	279	−8.71	−2	565.1	−101.3	−145.8
280	281	−9.03	9	531.2	−206.5	Non
283	284	−9.08	7	572.1	−211.4	Non
293	294	−8.62	−4	598.3	−150.2	−177.33
319	320	−8.71	24	522.8	−193.7	Non
313	314	−0.06	10	391.3	−34.2	−42.0
314	315	−0.28	0	380.4	−1.9	−10.6
338	339	−0.36	5	431.2	−51.3	−70.9
339	340	−0.47	−22	509.1	64.5	89.4
340	341	−0.16	−13	485.6	42.2	57.9
342	343	−0.62	6	457.7	−30.5	−53.5
343	344	−0.72	−1	348.8	6.1	6.7
344	345	0.07	1	456.6	35.7	42.9
345	346	−0.63	5	418.1	−62.0	−99.0
209	210	9.13	1	350.4	136.0	Non
210	211	9.18	−3	450.7	126.3	Non
211	212	9.13	2	463.8	149.1	Non
212	213	9.17	−2	434.3	88.0	133.1
213	214	8.80	0	617.5	112.8	167.2
214	215	9.16	−2	624.2	170.2	242.1
215	216	9.05	0	599.6	132.4	189.9
216	217	9.14	−1	622.4	138.0	203.2
217	218	9.40	0	511.2	187.8	Non

[1] D_{ac} is average value of D_{ci} ($i = 1, 2, 3$) that is defined in Fig. 9.

[2] D_{ag} is average value of D_{gj} ($j = 1, 2$) that is defined in Fig. 9.

[3] Non denotes that ground wires did not produce corresponding bright spots.

respectively. Table 2 shows the offsets of these bright spots $P_{i=1,2,3}$ in the extension direction of the power line. Here, D_{ac} represents the average value of $D_{ci}\,(i = 1, 2, 3)$ and D_{ag} the average value of $D_{gj}\,(j = 1, 2)$.

The following results can be gleaned from Table 2.

a) When $\alpha \approx -9°$, D_{ac} is negative. In addition, when $H_{BA} \geq 0\,\text{m}$, two ground wires did not produce corresponding bright spots. Moreover, when $H_{BA} < 0\,\text{m}$, D_{ag} is also negative, and its absolute value is larger than that of D_{ac}.

b) When $\alpha \approx 0°$, but negative, if $H_{BA} \geq 0\,\text{m}$, D_{ac} and D_{ag} are negative. On the contrary, if $H_{BA} < 0\,\text{m}$, both D_{ac} and D_{ag} change to positive values. However, when α is positive, D_{ac} and D_{ag} are positive, regardless of whether H_{BA} is positive. In addition, the absolute value of D_{ag} is larger than that of D_{ac} in this case.

c) When $\alpha \approx 9°$, four groups of ground wires did not produce corresponding bright spots. For the other five groups of ground wires, D_{ag} is larger than D_{ac}. In addition, when both α and H_{BA} remain constant, such as the pylons numbered (212–213) and (214–215), respectively, a larger span length can result in larger values of D_{ac} and D_{ag}.

5. DISCUSSION

When a TerraSAR-X satellite operating in the X band is employed to detect UHV power lines, since the surface fluctuation of a sub-conductor is less than 1.2 mm, which is much smaller than the wavelength of the X-band SAR, the surface of the sub-conductor can be considered to be smooth. Considering the very long distance between the SAR satellite and transmission line, as well as the practical shape of the UHV power line, it reflects the radar signal like a smooth arc. As expected, the observation results demonstrate that the radar backscatter response of the UHV power line is dominated by the specular reflections when a TerraSAR-X satellite is used as illumination, which is similar to the case with airborne millimeter-wave SAR [25, 26], although the geometry between them is different. However, it is difficult to determine what proportion of the UHV power line reflects the radar signal, although the satellite orbit and imaging geometry are known. This is due to the varying incidence angle during the synthetic aperture, as well as the fact that the intensity of the received signal changes with the specular reflections from different parts of the sagging power line, as shown in Fig. 8. In addition, different from long-distance linear ground objects, which usually appear as bright lines in a spaceborne SAR image, such as highways [27] and railroad lines [28], each section of UHV power lines produces a bright spot in the TerraSAR-X imagery because of the conductor sag, similar to the case of a corner reflector [29]. Furthermore, due to the different geometries, the scattering characteristics of a UHV power line in a TerraSAR-X image are also different from those in an airborne SAR image, in which the power line appears as a bright line [30].

It can be seen from Fig. 7 that when the extension direction of the power line is consistent with the azimuth of the sub-satellite ground track, i.e., $\alpha \approx 0^\circ$, a large part of signals scattered by the power line can be received by the radar that is carried by the TerraSAR satellite because of the specular reflection of the power line. However, when the absolute value of α exceeds 15°, only a small part of the signals scattered by the power line can be received by the TerraSAR-X satellite, resulting in a low echo signal strength, and hence the power line cannot produce a bright spot in the TerraSAR-X image. Nevertheless, when $-10^\circ \leq \alpha \leq 10^\circ$, four sections of power lines did not produce the corresponding bright spots. This means that, besides angle α, other factors can also influence the generation of these bright spots, such as H_{BA}, as shown in Table 2. In practical operation, one can judge whether a UHV power line is disconnected based on the appearance of the bright spots on time-series TerraSAR-X images.

As described in Section 4.1, the intensity of the bright spots produced by a UHV power line varies between 56 and 76 dB, which is larger than that of the bright spots generated by an EHV power line [12], because the diameter of a UHV power line is larger than that of an EHV power line. When bright spots produced by a power line appear in a TerraSAR-X image, however, those produced by the ground wires cannot be found in some cases, as shown in Table 2. This is because the radar cross-section of conductor bundles is larger than that of the ground wire, as shown in Fig. 3. In addition, since the diameters of a sub-conductor and a ground wire are 30 and 17 mm, respectively, the section of the conductor bundles is 14 times larger than that of the ground wire. As a result, the theoretical difference between their scattering intensities is approximately 11 dB, which is consistent with the practical difference of 10 dB.

Table 2 shows that, besides L_s, the spatial location of bright spots in a TerraSAR-X image is also influenced by α and H_{BA}. For different values of α, the part of the power line that reflects the radar signal is different, which results in the variation of the spatial location of the bright spots in a TerraSAR-X image. Moreover, since H_{BA} can change the shape of the power line, the part of the power line that reflects the radar signal also varies with H_{BA}, which further causes the variation of the spatial location of the bright spots in a TerraSAR-X image. Since both span length and H_{BA} are related to the conductor sag, it can be concluded that the spatial location of the bright spots produced by a power line is influenced by the conductor sag. Therefore, one can judge whether the conductor sag is within the specified range by analyzing the spatial location of the bright spots in a TerraSAR-X image in practical operation.

6. CONCLUSION

As a first step to accurately explain the scattering characteristics of UHV power lines in spaceborne SAR images and to achieve the effective monitoring of wide-area UHV power lines in adverse weather conditions using spaceborne SAR images, this paper proposes a data processing method used to extract power lines from spaceborne SAR images and analyzes the practical scattering characteristics of UHV power lines in 3-m-resolution TerraSAR-X images collected over the study area. The analysis results demonstrate that the radar backscatter response of the UHV power line is dominated by the specular reflections when a TerraSAR-X satellite is used as illumination. Furthermore, a UHV power line can be visible in a TerraSAR-X image only when the angle between the extension direction of the power line and the azimuth of the sub-satellite ground track is within ±15°. In addition, the spatial location of a UHV power line in a TerraSAR-X image is influenced by the angle between the extension direction of the power line and the azimuth of the sub-satellite ground track, as well as the conductor sag. It is worth mentioning here that the same conclusions were obtained using the 3-m-resolution COSMO-SkyMed images collected over the same study area, whose illuminating property is different from that of the TerraSAR satellite. In future work, on the one hand, several algorithms will be developed for the effective monitoring of UHV power lines in adverse weather conditions using TerraSAR-X images. On the other hand, the electromagnetic scattering characteristics of a UHV power line will be studied for spaceborne SAR operating separately in the X, C, and L bands, which includes the effects of several parameters of practical importance on the backscatter behavior of UHV power lines such as the incidence angle, polarization type, height difference between adjacent pylons, conductor sag, cable diameter, and aspect angle of illumination [31, 32]. Furthermore, when spaceborne SAR is adopted to monitor UHV power lines, the simulation of its echo will be performed to accurately explain the generation of the bright spots in a spaceborne SAR image, similar to the study described in [33].

ACKNOWLEDGMENT

This research was funded by Open Fund of State Key Laboratory of Power Grid Environmental Protection (No. GYW51201901073). We would like to thank the anonymous reviewers for their helpful comments and suggestions, and thank LetPub (www.letpub.com) for its linguistic assistance during the preparation of this manuscript.

REFERENCES

1. Huang, D., Y. Shu, J. Ruan, and Y. Hu, "Ultra high voltage transmission in China: Developments, current status and future prospects," *Proceedings of the IEEE*, Vol. 97, No. 3, 555–583, Mar. 2009.
2. Wen, C., W. Li, T. Chen, J. Chen, and J. Liu, "The patrol inspection technology for UHV transmission lines based on the UAV technology," *The 1st International Conference on Big Data Analytics for Cyber-Physical System in Smart City (BDCPS)*, 1600–1606, Shenyang, China, Dec. 2019.
3. Nie, D., R. Huang, F. Zhou, et al., "Fault characteristics analysis of transmission lines with foreign bodies based on satellite remote sensing images," *Shandong Electric Power*, Vol. 46, No. 8, 77–80, 2019.
4. Awrangjeb, M., "Extraction of power line pylons and wires using airborne LiDAR data at different height levels," *Remote Sensing*, Vol. 11, No. 15, 1798, Aug. 2019.
5. Goshi, D. S. and L. Q. Bui, "Power line characterization from an airborne data collection with a millimeter wave radar," *Radar Sensor Technology XVIII*, Baltimore, MD, United States, May 2014.
6. Chen, S., Z. Wang, and J. Zhao, "Spaceborne SAR technology application in the smart grid," *67th International Astronautical Congress (IAC)*, Guadalajara, Mexico, Sep. 2016.
7. Matikainen, L., M. Lehtomaki, E. Ahokas, et al., "Remote sensing methods for power line corridor surveys," *ISPRS J. Photogramm. Remote Sens.*, Vol. 119, 10–31, Sep. 2016.

8. Schwarz, G., M. Soccorsi, H. Chaabouni-Chouayakh, et al., “Automated information extraction from high resolution SAR images: TerraSAR-X interpretation applications,” *International Geoscience and Remote Sensing Symposium (IGARSS)*, Vol. 4, IV677–IV680, Cape Town, South Africa, Jul. 2009.
9. Liu, Y., A. Hou, S. Li, et al., “High voltage power line scattering feature analysis in multi SAR sensors and dual polarization,” *2nd International Workshop on Earth Observation and Remote Sensing Applications (EORSA)*, 225–229, Shanghai, China, Jun. 2012.
10. Liu, Y., Y. Hu, L. Wang, K. Liu, et al., “Surveillance for 1000 kV transmission tower deformation using high-resolution SAR satellite,” *High Voltage Engineering*, Vol. 35, No. 9, 2076–2080, Sep. 2009.
11. Li, T., L. Chen, Y. Liu, et al., “Ultra high voltage power tower SAR interferometry and icing tower testing results,” *6th Asia-Pacific Conference on Synthetic Aperture Radar (APSAR)*, 1–5, Xiamen, China, Nov. 2019.
12. Li, S., T. Li, M. Wang, et al., “Study on extra-high voltage power line scatterers in time series SAR,” *3rd International Workshop on Earth Observation and Remote Sensing Applications (EORSA)*, 47–51, Changsha, China, Oct. 2014.
13. Chen, Z., T. Li, X. Zhang, et al., “Analysis on time series phase stability of power line scatterers in SAR images,” *Engineering of Surveying and Mapping*, Vol. 26, No. 4, 22–26, Apr. 2017.
14. Zeng, Q., “Study on characteristics of maximum power frequency electric field gradient on ground and maximum sag of bundle conductor for UHVAC transmission line,” *Power System Technology*, Vol. 32, No. 6, 1–7, Mar. 2008.
15. Tao, W. and Y. Liu, “Simulation method of high-resolution spaceborne SAR imaging for the South-to-North transmission line,” *J. Comput. Methods Sci. Eng.*, Vol. 17, No. 3, 569–579, 2017.
16. Liu, Y., K. Xu, S. Shi, and T. Li, “Effects of span length and radar polarimetry on the backscattering characteristics of ultra-high voltage power transmission line in TerraSAR-X images,” *5th International Workshop on Earth Observation and Remote Sensing Applications (EORSA)*, 1–5, Xi’an, China, Dec. 2018.
17. Sarabandi, K. and M. Park, “Extraction of power line maps from millimeter-wave polarimetric SAR images,” *IEEE Transactions on Antennas and Propagation*, Vol. 48, No. 12, 1802–1809, Dec. 2000.
18. Deng, P., P. Li, J. Zhang, and J. Yang, “Power line detection from synthetic aperture radar imagery using coherence of co-polarisation and cross-polarisation estimated in the Hough domain,” *IET Radar, Sonar, and Navigation*, Vol. 6, No. 9, 873–880, 2012.
19. Han, X., X. Sun, H. Chen, et al., “The overview of development of UHV AC transmission technology in China,” *Zhongguo Dianji Gongcheng Xuebao*, Vol. 40, No. 14, 4371–4386, 2020.
20. Liang, Z., Y. Li, H. Hu, and J. Jia, “Design of UHV AC transmission line in China,” *European Transactions on Electrical Power*, Vol. 22, No. 1, 4–16, 2012.
21. Breit, H., T. Fritz, U. Balss, et al., “TerraSAR-X SAR processing and products,” *IEEE Transactions on Geoscience and Remote Sensing*, Vol. 48, No. 2, 727–740, Feb. 2010.
22. Yan, W., S. Shi, L. Pan, et al., “Unsupervised change detection in SAR images based on frequency difference and a modified fuzzy C-means clustering,” *International Journal of Remote Sensing*, Vol. 39, No. 10, 3055–3075, May 2018.
23. Cheney, M., “A mathematical tutorial on synthetic aperture radar,” *SIAM Review*, Vol. 43, No. 2, 301–312, Jun. 2001.
24. Li, S., T. Li, M. Wang, et al., “Analysis on scatters time series of extra-high voltage power line,” *Science of Surveying and Mapping*, Vol. 40, No. 4, 126–130, Apr. 2015.
25. Xia, Y., H. Kaufmann, and X. Guo, “Differential SAR interferometry using corner reflectors,” *International Geoscience and Remote Sensing Symposium (IGARSS)*, 1243–1246, Toronto, Ontario, Canada, 2002.
26. Willetts, B., M. B. Stevens, A. G. Stove, and M. S. Gashinova, “Spectrum analysis of high-resolution SAR data to obtain Bragg signatures of power cables,” *IET Radar, Sonar, and Navigation*, Vol. 12, No. 8, 839–843, May 2018.

27. Sarabandi, K. and M. Park, "A radar cross-section model for power lines at millimeter-wave frequencies," *IEEE Transactions on Antennas and Propagation*, Vol. 51, No. 9, 2353–2359, Sep. 2003.
28. Dai, K., G. Liu, Z. Li, et al., "Monitoring highway stability in Permafrost regions with X-band temporary scatterers stacking InSAR," *Sensors*, Vol. 18, No. 6, 1876, Jun. 2018.
29. Acar, S. A. and S. Bayir, "Detection of railroad networks in SAR images," *International Journal of Advanced Computer Science and Applications*, Vol. 9, No. 9, 133–138, 2018.
30. Essen, H., S. Boehmsdorff, G. Biegel, and A. Wahlen, "On the scattering mechanism of power lines at millimeter-waves," *IEEE Transactions on Geoscience and Remote Sensing*, Vol. 40, No. 9, 1895–1903, Sep. 2002.
31. Liu, Y., K. Liu, S. Shi, and K. Xu, "Electromagnetic scattering characteristics of ultra-high-voltage power transmission line at X-band frequencies," *Journal of Harbin Institute of Technology*, Vol. 52, No. 3, 173–178, Mar. 2020.
32. Shi, S., Y. Liu, L. Cheng, and Z. Chen, "Numerical simulation of the electromagnetic scattering characteristics of ultra-high voltage power line at X-band," *IEEE 6th International Conference on Computer and Communications (ICCC)*, 2289–2293, Chengdu, China, Dec. 2020.
33. Yue, H., B. Hu, and R. Yang, "Research on spaceborne SAR raw data simulation," *2006 CIE International Conference on Radar*, 1–4, Shanghai, China, Oct. 2006.